



## Full Text View

[Volume 32, Issue 1 \(January 2002\)](#)

### Journal of Physical Oceanography

Article: pp. 161–176 | [Abstract](#) | [PDF \(1.38M\)](#)

# A Series of Middepth Zonal Flows in the Pacific Driven by Winds

**Hideyuki Nakano and Nobuo Suginozara\***

*Center for Climate System Research, University of Tokyo, Tokyo, Japan*

(Manuscript received December 5, 2000, in final form June 11, 2001)

DOI: 10.1175/1520-0485(2002)032<0161:ASOMZF>2.0.CO;2

### ABSTRACT

A series of middepth zonal flows observed in the Pacific is produced in a World Ocean model with the horizontal resolution of  $1^\circ \times 1^\circ$  and 40 vertical levels. It is demonstrated that the middepth zonal flows are driven by the wind and reach down to several thousand meters. The surface wind gyres appear to shift poleward with depth, leaving behind the gyres that originate from the equatorial response. In meridional sections, the pattern of the zonal flows slants poleward with increasing depth. The formation mechanism for the middepth zonal flows is clarified using an idealized basin model and a semianalytical model of vertical normal mode decomposition. In the models, the inclusion of vertical diffusion is essential. The zonal flows at low latitudes are formed as the equatorial response to uniform zonal winds. The response at middle and high latitudes is accounted for as follows. Quasigeostrophic (QG) dynamics with vertical diffusion reproduces the reversal of the zonal flows with depth. The slanting pattern of the zonal flows is due to the non-QG effect for the response of the vertical higher modes. Then the inclusion of horizontal diffusion reduces the response of the gravest modes. The third to fifth vertical modes are very important for forming the middepth wind-driven circulation. The wind-driven circulation at middepths is very weak compared to that in the surface layer, but this is sufficient to overcome the weak thermohaline circulation in the middepth Pacific.

#### Table of Contents:

- [Introduction](#)
- [World Ocean model](#)
- [Rectangular basin model](#)
- [Discussion and concluding](#)
- [REFERENCES](#)
- [TABLES](#)
- [FIGURES](#)

#### Options:

- [Create Reference](#)
- [Email this Article](#)
- [Add to MyArchive](#)
- [Search AMS Glossary](#)

#### Search CrossRef for:

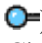
- [Articles Citing This Article](#)

#### Search Google Scholar for:

- [Hideyuki Nakano](#)
- [Nobuo Suginozara](#)

## 1. Introduction

Our knowledge of the circulation below the thermocline is limited compared to that of the upper ocean. Swift deep western boundary currents associated with the thermohaline circulation are relatively well observed, and their path and strength are becoming gradually clear. On the other hand, farther from the western boundary, little is known about circulations owing to their slow flow speed.

From the Geochemical Ocean Sections Study and World Ocean Circulation Experiment, [Lupton \(1998\)](#) summarized the  $\delta^3\text{He}$  distribution and the flow pattern derived from it at middepths in the eastern Pacific. At 2500-m depth the strongest maximum in  $\delta^3\text{He}$  at  $12^\circ\text{--}13^\circ\text{S}$  extends from the East Pacific Rise helium plume, a weaker maximum extends eastward at  $28^\circ\text{S}$ , and a slightly weaker maximum extends westward centered at  $8^\circ\text{N}$ . Besides, a minimum lies on the equator between the nearly symmetric maxima. The first maximum signal indicates westward flow, the second one eastward flow, the third one westward flow, and the last minimum eastward flow. At 2000-m depth, the helium signal from the Juan de Fuca Ridge indicates westward flow at  $35^\circ\text{N}$ . At 1100-m depth, the helium signal extends eastward from Loihi Seamount south of Hawaii, indicating eastward flow around  $20^\circ\text{N}$ . The distribution of middepth zonal flows derived from  $^3\text{He}$  measurements in the eastern Pacific is consistent with that of [Reid's \(1997\)](#) adjusted steric height map on 2500 db, although the westward flow at 2000 m and the eastward flow at 1100 m cannot be directly compared ([Fig. 1](#) ). The westward flow at  $12^\circ\text{--}13^\circ\text{S}$  also appears in [Davis' \(1998\)](#) geostrophic pressure map from Autonomous Lagrangian Circulation Explorer floats data at 900 m.

In addition to the helium signals, there is evidence to support the existence of the middepth zonal flows in the Pacific. [Talley and Johnson \(1994\)](#) found large-scale, westward-extending tongues of the warm water between 2000 m and 3000 m both north and south of the equator, centered at  $5^\circ\text{--}8^\circ\text{N}$  and  $10^\circ\text{--}15^\circ\text{S}$ . Zonal flows are observed also at high latitudes in the North Pacific. With current meters, [Warren and Owens \(1985\)](#) observed westward flow just south of the Aleutian Island Arc and a strong eastward flow south of this along  $175^\circ\text{W}$  at 3000-m depth. These are also consistent with [Reid's \(1997\)](#) adjusted steric height map. Therefore, there seems to exist a series of middepth zonal flows in the Pacific. However, it had not been noted in World Ocean models, and its formation mechanism was unknown.

It is commonly believed that the deep circulation below the thermocline is mainly driven by the thermohaline forcing, whereas the upper-layer circulation is mainly driven by the wind forcing. The most widely cited theory for the deep circulation is [Stommel and Arons' \(1960a,b\)](#), in which the circulation is described in a flat bottom ocean with horizontally uniform upwelling. According to the theory, the middepth circulation in the Pacific is thought to have the inverse Stommel–Arons pattern, that is, the flow is westward except at the equator and at the northern boundary, because the meridional overturning circulation in the Pacific has a layered structure (e.g., [Obata et al. 1996](#); [Tsujino et al. 2000](#)). Thus, the classical thermohaline circulation does not account for a series of middepth zonal flows.

It is known that topographic grounding can modify the abyssal circulation (e.g., [Speer et al. 1993](#)). [Warren and Owens \(1985\)](#) applied the Stommel–Arons theory to a one-layer model for the abyssal North Pacific (1000–5000 m), with constant thickness for  $0^\circ\text{--}45^\circ\text{N}$  and  $50^\circ\text{--}55^\circ\text{N}$ , and shallower northward for  $45^\circ\text{--}50^\circ\text{N}$ . The Stommel–Arons pattern modified by the topography shows a westward flow on the slope where the effective  $\beta$  is negative and a strong eastward flow north of it. They concluded that the strong eastward flow and the westward flow near the northern boundary correspond to the observed zonal flows. This may explain the swift current near the northern boundary. But it is not likely that the topographic grounding alone can cause the middepth zonal flows as there is not such a slope in other regions.

The distribution of  $^3\text{He}$  and other tracers may be interpreted as the active response to the thermal forcing of hydrothermal vents ([Stommel 1982](#); [Hautala and Riser 1993](#)). However, the strong thermal activities are not accompanied by strong flows ([Lupton 1998](#)), and there is a similar structure at lower latitudes in the Atlantic where such thermal activities do not exist ([Talley and Johnson 1994](#)). Thus, the hydrothermal vents are not likely the sole forcing agent for the middepth zonal flows, either.

A remaining agent for the zonal flows may be the wind forcing. Consider the response to the wind forcing in a two-layer model. When vertical diffusion is not considered, motion is confined to the upper layer while the lower layer stands still. This is the simplest idea of the wind-driven circulation in a stratified ocean. Therefore, the depths of the middepth zonal flows are usually assumed as a *state of rest* for the response to steady wind forcing in multilayer models. In addition, this assumption is used as the constraint to obtain an analytical solution. However, when vertical diffusion is introduced, vertical higher mode Rossby waves, which set up the motionless abyssal layer, do not reach the western boundary, resulting in weak motion in the abyssal layer. This motion may account for the middepth flows although the distribution of them does not look correlated with that of the surface flows.

In this study, we produce a series of zonal flows in a  $1^\circ \times 1^\circ$  World Ocean model. Then, using an idealized basin model, we demonstrate that the wind forcing produces middepth zonal flows, and their formation mechanism in this model is clarified.

This paper is organized as follows. In [section 2](#), an experiment is carried out using an ocean general circulation model (OGCM). Comparing the results of the OGCM with the observed flows, we show that a series of middepth zonal flows is reproduced realistically in the OGCM and indicate that it is caused by the wind forcing. In [section 3](#), we reproduce the middepth zonal flows in an idealized basin model with vertical and horizontal diffusion as the response to the wind forcing. Then, using the method of vertical normal mode decomposition, the formation mechanism is clarified semianalytically.

Sensitivity experiments with different vertical and horizontal diffusivity are also carried out. [Section 4](#) is a discussion and concluding remarks.

## 2. World Ocean model

### a. Experimental design

In this study, we use the Center for Climate System Research (CCSR) Ocean Component model (COCO) described by [Hasumi \(2000\)](#). The model has isopycnal diffusion with weak background horizontal diffusion. A high-accuracy tracer advection scheme, UTOPIA ([Leonard et al. 1993, 1994](#)), is incorporated. UTOPIA has third-order accuracy with little numerical diffusion and dispersion. The performance of COCO with UTOPIA is described by [Hasumi and Sugimoto \(1999a\)](#). The [Gent and McWilliams \(1990\)](#) parameterization (hereafter GM parameterization) for mesoscale eddies and also a bottom boundary layer model are introduced in the model. The horizontal resolution is  $1^\circ \times 1^\circ$  and there are 40 levels in the vertical with high resolution near the sea surface (50 m) and decreasing resolution toward the bottom (200 m). The model domain is global, but the Arctic Ocean is excluded for computational efficiency. Surface forcings are seasonally varying. The wind stress is taken from [Hellerman and Rosenstein \(1983\)](#). Following [Haney \(1971\)](#), the sea surface temperature is restored to “apparent atmosphere temperature,” which is derived from longwave radiation, shortwave radiation, and latent and sensible heat flux from [da Silva et al. \(1994\)](#). Salinity flux, which corresponds to evaporation minus precipitation ( $E - P$ ) from [da Silva et al. \(1994\)](#), is imposed. In addition, the sea surface salinity is weakly restored to the monthly mean value of [Levitus and Boyer \(1994\)](#) with a damping time of 200 days to avoid climate drift. For time interpolation of these sea surface data, the method of [Killworth \(1996\)](#) is used so that the values imposed on the model equal those of the original monthly datasets when averaged over a month. We adopt [Tsujino et al.'s \(2000\)](#) vertical diffusivity, which takes the value of  $0.1 \times 10^{-4} \text{ m}^2 \text{ s}^{-1}$  at the upper thermocline depths,  $1.0 \times 10^{-4} \text{ m}^2 \text{ s}^{-1}$  at the lower thermocline depths, and a larger value of  $2.7 \times 10^{-4} \text{ m}^2 \text{ s}^{-1}$  in the bottom layer. Following the method of [Danabasoglu et al. \(1996\)](#), the model is integrated with seasonally varying surface forcings for more than ten thousand years of accelerated integration ([Bryan 1984](#)) followed by thirty years of synchronous integration. The results presented below are the annual mean for the last year of synchronous integration. The detailed setup of the model is described in [Nakano and Sugimoto 2002](#), hereafter NSa.

### b. Results

#### 1) BASIC STRUCTURE IN THE DEEP PACIFIC

General features of basic structures in the deep Pacific are described by [Nakano and Sugimoto \(2001\)](#), hereafter NSb). Here, we show how well the thermohaline circulation and the basic stratification are formed in the model Pacific. The thermohaline circulation can be represented by the zonally integrated meridional transport streamfunction (meridional overturning circulation). [Figure 2](#) shows the meridional overturning circulation in the Pacific. About 8 Sv ( $\text{Sv} \equiv 10^6 \text{ m}^3 \text{ s}^{-1}$ ) of Circumpolar Deep Water enters the North Pacific, which is nearly the same as the observed value (e.g., [Roemmich et al. 1996](#)). This forms the layered structure, with northward transport at the bottom and southward transport at middepths (e.g., [Obata et al. 1996](#); [Tsujino et al. 2000](#)). Accordingly, the horizontal circulation at middepths ( $\sim 2000 \text{ m}$ ) has the inverse Stommel–Arons pattern with a broad interior westward flow except at the equator and in the western boundary region. [Figure 3](#) shows the vertical profiles of horizontally averaged potential density ( $\sigma_2$ ) in the North Pacific for the model and the annual mean climatology of [Levitus and Boyer \(1994\)](#). The potential density is well reproduced in the model although it is slightly light for the upper thermocline and slightly heavy for the lower thermocline. On the whole, the deep Pacific is realistically reproduced at least in terms of its horizontally averaged profile.

#### 2) MIDDEPTH ZONAL FLOWS

##### (i) Comparison with observation

[Figure 4](#) shows the distribution of zonal flows at 2405-m depth for the model. The modeled circulation is quite different from the inverse Stommel–Arons pattern. A series of middepth zonal flows suggested by [Lupton \(1998\)](#) and [Reid \(1997\)](#) is well reproduced: it consists of the eastward flow at the equator, westward flows around  $10^\circ$ , eastward flows around  $20^\circ$ , and westward flows around  $30^\circ$  at 2500-m depth. The number and latitudes of the alternating zonal flows are similar to the observed (cf. [Fig. 4](#) with [Fig. 1](#)). The eastward flow at the equator is part of a set of vertically alternating zonal jets along the equator discussed later.

In [Reid's \(1997\)](#) adjusted steric height maps, the surface wind gyres shift poleward with depth, leaving behind new gyres in the Tropics. [Figure 5](#) shows the pressure fields at 500, 1000 m, and 1500 m in the model. We can see that the modeled pattern also shifts poleward with increasing depth. Although the eastward flow around  $20^\circ\text{N}$  is not clearly seen at 2500 m ([Fig. 4](#)), the band of eastward flow appears from Mindanao to the Baja California Peninsula at 1000 m and 1500

m. The eastward flow at 1000-m depth represents the helium signal extending eastward from Loihi Seamount (Lupton 1998). The tropical cyclonic circulation centered 10°S at 1000-m depth is found both in Reid's (1997) map on 1000 db and the Davis (1998) geostrophic pressure map at 900 m.

Next, let us look at the meridional section to more clearly see changes in distribution of the zonal flows with depth. Figure 6 shows the meridional sections of zonal flows along 170°E and 140°W. At 2500-m depth, a series of zonal flows is clearly seen, and its latitudinal distribution is consistent with the observed helium signal. At depth 2000–2500 m in the eastern Pacific, Lupton (1998) showed eastward flow at 28°S, 20°N, and the equator and westward flow at 13°S, 8°N, 35°N, and north and south of the equator. There are also westward flow just south of the Aleutian Island Arc and eastward flow south of it along 170°E at 3000-m depth, which are indicated by the current meters (Warren and Owens 1985). These observed flows are so swift ( $1\text{--}3\text{ cm s}^{-1}$ ) that the modeled flows may not correspond to the observed, presumably due to the lack of the proper representation of the topography, which may create such flows (Warren and Owens 1985). But, at least, the directions and latitudes of the flows are consistent. Examination of the flow structure between 140°W and 170°E indicates that the middepth zonal flows are not bottom trapped. The pattern of the zonal flows has the following characteristics: the zonal flows change their direction with depth, particularly at lower latitudes, and their pattern slants poleward with increasing depth. The formation mechanism is discussed in the next section.

In the tropical region, in addition to the Equatorial Undercurrent, eastward flows at the pycnocline depth are formed around 5° in both hemispheres. Also, along the equator a set of vertically alternating zonal jets, “stacked jets,” is found associated with the thermohaline circulation (Suginohara and Fukasawa 1988; Suginohara and Aoki 1991; Suginohara et al. 1991). Yamanaka et al. (2000) reproduced the stacked jets in a model with 800 vertical levels, and Furue (2001) obtained them as analytical solutions of the equatorial diffusive boundary layer. The stacked jets in the present model are caused by effects of the large vertical diffusivity in the deep layers (NSb). These flows are different from the vertically alternating zonal jets observed by Firing (1987) at depth 500–2000-m, but one of them corresponds to the eastward flow obtained by Johnson and Toole (1993) on the equator at 2000–2500 m for 2°S–2°N along 165°E.

On the whole, the series of observed middepth zonal flows is well reproduced. Effects of hydrothermal vents are not included in the present model. Therefore, the influence of hydrothermal vents on the circulation may be small in the real ocean as suggested by Talley and Johnson (1994).

#### (ii) Experiment with no wind forcing in the Pacific

In the meridional sections, the latitudinal distribution of the middepth flows seems to be traced to the surface wind gyres rather than to the bottom-trapped flows. To understand the effects of winds on the middepth zonal flows, we carried out another experiment where no wind forcing is imposed in the Pacific for 80 yr starting from the equilibrium state. Figure 7 shows the difference in zonal flow between the cases with and without the Pacific winds. A series of middepth zonal flows appears in the wind-forced case, whereas the stacked jets along the equator and the bottom-trapped flows appear in both experiments. Therefore, the middepth zonal flows are caused by the wind forcing.

There may be various effects in the wind forcing. Since the thermohaline forcing may dominate in the deep layers, the middepth flows could be the thermohaline circulation modified by the wind forcing. However, it is demonstrated in the next section that the middepth zonal flows are due solely to the wind forcing, which reaches down to several thousand meters.

### 3. Rectangular basin model

#### a. Response of the Pacific to wind forcing

We consider a rectangular ocean whose latitudinal and longitudinal domain are 40°S–60°N and 120°W–0°, respectively. The bottom is flat and 5900 m deep. The horizontal resolution is  $2^\circ \times 2^\circ$ , and the vertical resolution is the same as that of the World Ocean model.

The initial stratification is uniform in both latitude and longitude, derived from the horizontally averaged modeled temperature-salinity in the North Pacific. The surface temperature-salinity is restored to the constant initial value with a restoring time of 30 days. The zonally averaged steady wind stress in the Pacific is imposed. The lateral boundaries are insulated; that is, the abyssal flow that enters from the south is ignored. The vertical diffusivity is the same as used in the World Ocean model. The model is integrated for 100 years so that spin up of the wind-driven circulation is completed. There is no significant meridional overturn in the abyssal layer. This experiment will serve as the control experiment for sensitivity experiments discussed in section 3d.

Figure 8 shows the horizontal distribution of the zonal component of velocity at 2405-m depth for the rectangular basin model, along with that of the difference in zonal flow between the cases with and without the Pacific winds for the

World Ocean model. The zonal flows for the two models are strikingly similar in the horizontal distribution. These resultant zonal flows seem western intensified, consistent with the arguments in the semianalytical solution discussed later. However, when the thermohaline circulation is included, the wind-driven intensified zonal flows may not appear clearly due to the overlapping thermohaline circulation, as seen in [Fig. 4](#).

Although these horizontal distributions of flows for the two cases are similar, the zonal flows for the rectangular basin model are weaker than those for the World Ocean model. One reason for the difference is that the depth of the rectangular basin model (5900 m) is greater than the zonally averaged depth at each latitude for the World Ocean model (4000–5000 m), resulting in weaker vertical diffusion for the rectangular basin since diffusion is inversely proportional to the fourth power of the propagation speed of gravity waves (see [section 3c](#)). This tendency is significant for the South Pacific where the depths are relatively shallower. Note that stronger diffusion results in a stronger middepth circulation, which will be explained later.

[Figure 9](#) depicts the meridional sections for the zonal flows along 90°W and 30°W for the rectangular basin model. The meridional distribution of the zonal flows for the rectangular basin is also similar to that of the difference in zonal flow between the cases with and without Pacific winds for the World Ocean model (cf. [Fig. 9](#) with [Fig. 7](#)). Thus, the middepth zonal flows obtained in the World Ocean model can be explained as the response to the wind forcing. Next, we present an analytical theory for the middepth zonal flows. The response of the equatorial region and that of the middle and high latitudes are discussed in turn.

### b. Response of the equatorial region to wind forcing

We first discuss the equatorial response. [Figure 10](#) depicts the response to a uniform zonal wind stress of  $-4.0 \times 10^{-2} \text{ N m}^{-2}$ . The distribution of the zonal flows in the equatorial region is similar to that in [Fig. 9a](#). As already seen, in addition to the Equatorial Under-current, eastward flows at the pycnocline depth are formed around 5° in both hemispheres. These currents were modeled by [McCreary \(1981\)](#) and [Kitamura and Sugimoto \(1987\)](#), who also clarified their dynamics. The equatorial response also creates flows at middle and high latitudes through coastal Kelvin waves and Rossby wave dispersion. But, away from the eastern boundary, the flows at middle and high latitudes are much weaker than those in [Fig. 9a](#), implying that the equatorial response does not contribute much to the flows at middle and high latitudes.

### c. Response of the middle and high latitudes to wind forcing

Next, we discuss the midlatitude North Pacific response. To eliminate the equatorial response, the zonal wind stress is modified as

$$\tau_0(y) = 6.0 \times 10^{-2} \times \left[ \cos\left(\frac{2\pi(y - y_1)}{\lambda}\right) + 1 \right] \quad (\text{N m}^{-2}) \quad (y \geq 20^\circ\text{N}), \quad (1)$$

where  $y_1$  and  $\lambda$  are 40°N and 40°, respectively. There is no wind stress south of 20°N. This idealized wind stress [\(1\)](#) reproduces the subtropical and subpolar gyres of the North Pacific although the gyre boundary is shifted slightly southward (3° ~ 5°) and the subpolar gyre becomes strong compared with the World Ocean model. [Figure 11](#) shows the response to this zonal wind stress. The distribution of zonal flows captures the structure shown in [Fig. 9a](#) at middle and high latitudes, indicating that the zonal flows at middle and high latitudes are formed as the response to the winds.

Next, we obtain semianalytical solutions for the midlatitude interior response using vertical normal mode decomposition.

#### 1) SEMIANALYTICAL MODEL


Consider a set of linearized equations for a continuously stratified interior ocean on a  $\beta$ -plane in steady state:

$$\frac{\partial u}{\partial x} + \frac{\partial v}{\partial y} + \frac{\partial w}{\partial z} = 0, \quad (4)$$

$$-\frac{\rho_0 N^2 w}{g} = \frac{\partial^2}{\partial z^2} (K_v \rho'), \quad (5)$$

$$\frac{\partial p'}{\partial z} = -\rho' g, \quad (6)$$

$$N^2 \equiv -\frac{g}{\rho_0} \frac{d\bar{\rho}}{dz}, \quad (7)$$

where  $u$ ,  $v$ , and  $w$  are the zonal, the meridional, and the vertical component of velocity, respectively, and  $p'$  and  $\rho'$  are the pressure and the density anomaly from the state of no motion,  $\rho_0$  is the characteristic value of density,  $g$  is acceleration due to gravity,  $f$  is the Coriolis parameter,  $N$  is buoyancy frequency,  $F$  and  $G$  are the external driving forcings in the zonal and the meridional direction, respectively, and  $K_v$  is the coefficient of vertical diffusion;  $\bar{\rho}(z)$  is the basic stratification, which is the same as the modeled horizontal mean in the Pacific (Fig. 3 )

When  $K_v$  is assumed to be inversely proportional to  $N^2$ , the dependent variables can be expanded into the vertical normal modes (McCreary 1981):

$$u(x, y, z) = \sum_n \frac{\hat{p}_n(z)}{\rho_0 g} \tilde{u}_n(x, y), \quad (8)$$

$$v(x, y, z) = \sum_n \frac{\hat{p}_n(z)}{\rho_0 g} \tilde{v}_n(x, y), \quad (9)$$

$$p'(x, y, z) = \sum_n \hat{p}_n(z) \tilde{\eta}_n(x, y), \quad (10)$$

where  $\hat{p}_n(z)$  is the eigenfunction for the equation,

$$\frac{d}{dz} \left( \frac{1}{N^2} \frac{d\hat{p}_n}{dz} \right) = -\frac{\hat{p}_n}{c_n^2}, \quad (11)$$

$$\frac{d\hat{p}_n}{dz} = 0 \quad \text{at } z = 0 \quad \text{and} \quad -H, \quad (12)$$

where  $H$  is the depth of the flat bottom ocean, take as 5900 m. The subscript  $n$  denotes the mode numbers, with the  $n = 0$  ( $n \geq 1$ ) mode corresponding to the barotropic (baroclinic) mode; the eigenvalue  $1/c_n^2$  is the inverse square of the propagation speed of gravity waves of the  $n$ th mode.

The governing equations become

$$H_n \left( \frac{\partial \tilde{u}_n}{\partial x} + \frac{\partial \tilde{v}_n}{\partial y} \right) = - \frac{K_v N^2}{c_n^2} \tilde{\eta}_n, \quad (15)$$

where the equivalent depth  $H_n = c_n^2/g$  is introduced. We set  $K_v N^2 = 1.0 \times 10^{-9} \text{ m}^2 \text{ s}^{-3}$  ( $K_v = 3.6 \times 10^{-5} \text{ m}^2 \text{ s}^{-1}$  at depth 475-m where  $N = 5.3 \times 10^{-3} \text{ s}^{-1}$ ).

A zonally uniform zonal wind stress is considered:

$$\tilde{F}_n(y) = \frac{\int_{-D}^0 \rho_0^{-1} \tau(y, z) \hat{p}_n dz}{\int_{-H}^0 \hat{p}_n^2 dz} = \tilde{\tau}_n(y), \quad (16)$$

$$\tilde{G}_n = 0, \quad (17)$$

$$\tau(y, z) = \begin{cases} \tau_0(y)/D, & z \geq -D \\ 0, & z < -D, \end{cases} \quad (18)$$


where  $D$  is the mixed layer depth. We set  $D = 50$  m.

Solutions to [Eqs. \(13\), \(14\), and \(15\)](#) are easily obtained without approximation by using the boundary condition  $\mathbf{\eta} = 0$  at  $x = 0$  (at the eastern boundary). But first, we discuss the solution when the quasigeostrophic (QG) approximation is made, which is

$$\tilde{u}_n = \frac{c_n^4}{K_v N^2 f^2} (e^{B_n x} - 1) \frac{\partial^2 \tilde{\tau}_n}{\partial y^2}, \quad (19)$$


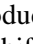
where  $B_n(y) \equiv K_v N^2 f^2 / \beta c_n^4$  and  $\beta \equiv df/dy$ . In the limit of no vertical diffusion, [\(19\)](#) corresponds to the well-known Sverdrup solution:

$$\tilde{u}_n = \frac{x}{\beta} \frac{\partial^2 \tilde{\tau}_n}{\partial y^2}. \quad (20)$$

[Figure 12](#)  depicts the zonal flow, which is the summation [\(8\)](#) of the solutions [\(19\)](#) along two meridional sections using [\(1\)](#) for the wind forcing. The QG solution produces the reversal of flow direction with depth, indicating that the higher modes are suppressed more efficiently in the west and at higher latitudes. However, the slanting pattern of the zonal flows is not reproduced.

Next, we obtain the solution to [Eqs. \(13\), \(14\), and \(15\)](#) without the QG approximation:

$$\tilde{u}_n = 2x e^{B_n x} \frac{\partial}{\partial y} \left( \frac{\tilde{\tau}_n}{f} \right) + \frac{c_n^4}{K_v N^2 f} (e^{B_n x} - 1) \frac{\partial^2}{\partial y^2} \left( \frac{\tilde{\tau}_n}{f} \right). \quad (21)$$

[Figure 13a](#)  depicts the zonal flow, superposition [\(8\)](#) of solution [\(21\)](#), along 90°W. The slanting pattern of the zonal flows is reproduced. [Figure 13b](#)  depicts the zonal flow for the  $n = 0, 1, 2$  modes and the  $n = 3$  mode, showing that the equatorward shift of the higher mode pattern creates the slanting pattern of the zonal flows.

To understand the equatorward shift with increasing mode number, we consider the limit of the fast and the slow wave speed for [\(21\)](#). For the fast wave-speed limit,  $B_n \rightarrow 0$ , [\(21\)](#) becomes

$$\bar{u}_n = 2x \frac{\partial}{\partial y} \left( \frac{\bar{\tau}_n}{f} \right) + \frac{fx}{\beta} \frac{\partial^2}{\partial y^2} \left( \frac{\bar{\tau}_n}{f} \right) = \frac{x}{\beta} \frac{\partial^2 \bar{\tau}_n}{\partial y^2}, \quad (22)$$

which is the same as the QG solution without vertical diffusion. Here there is no equatorward shift. On the other hand, when the wave speed is low, that is,  $B_n$  is large, the solution differs drastically between the region near the eastern boundary and the interior away from the eastern boundary. When  $|B_n x|$  is large, (21) becomes

$$\begin{aligned} \bar{u}_n &= -\frac{c_n^4}{K_v N^2 f} \frac{\partial^2}{\partial y^2} \left( \frac{\bar{\tau}_n}{f} \right) \\ &= -\frac{c_n^4}{K_v N^2 f} \left( \frac{1}{f} \frac{\partial^2 \bar{\tau}_n}{\partial y^2} - \frac{2\beta}{f^2} \frac{\partial \bar{\tau}_n}{\partial y} + \frac{2\beta^2}{f^3} \bar{\tau}_n \right). \end{aligned} \quad (23)$$

This is also the solution to [Eqs. \(13\), \(14\), and \(15\)](#) without an  $x$  derivative:

$$-f \bar{v}_n = \bar{\tau}_n, \quad (24)$$

$$f \bar{u}_n = -g \frac{\partial \bar{\eta}_n}{\partial y}, \quad (25)$$

$$H_n \frac{\partial \bar{v}_n}{\partial y} = -\frac{K_v N^2}{c_n^2} \bar{\eta}_n. \quad (26)$$

When  $B_n$  is large, Rossby waves from the eastern boundary do not propagate farther to the west. Therefore, away from the eastern boundary,  $f \bar{v}_n$  must be balanced by the local wind stress owing to the lack of zonal pressure gradient.

Solution (21) approaches solution (22) for the lower modes and solution (23) for the higher modes. Then, we evaluate the difference between the two solutions with respect to the latitude of zero zonal velocity. When the wind forcing is given by (1), (22) has  $u = 0$  at  $y = 30^\circ\text{N}$ . For (23),  $u = 0$  lies at about  $28^\circ\text{N}$ . Consequently, the zonal flow pattern shifts equatorward by about  $2^\circ$  for the higher modes. This results in the slanting pattern of the zonal flows as seen in [Fig. 13](#). Thus, for coarse resolution models of  $3^\circ \sim 5^\circ$ , it is difficult to resolve this shift. This is one of the reasons why the middepth zonal flows are not reproduced in the existing coarse resolution models.

Thus, the importance of vertical diffusion in creating the middepth zonal flows at a steady state is understood. Here, we consider the adjustment processes. When winds start to blow over a stratified ocean at rest, initially the ocean responds locally to the wind forcing without being affected by the boundaries. The setup for the vertical lower modes is accomplished when Rossby waves of corresponding modes from the eastern boundary arrive, which is presented by [Eq. \(22\)](#). For the higher modes, since Rossby waves cannot propagate farther to the west due to damping caused by the vertical diffusion, the adjustment is completed locally by the effect of vertical diffusion, which is presented by [Eq. \(23\)](#). The adjustment time of Rossby waves,  $\tau_R$ , is of order  $Lf^2/(\beta c_n^2)$ , and that of the vertical diffusion,  $\tau_D$ , is of order  $c_n^2/(K_v N^2)$ , where  $L$  is the longitudinal length of the domain. In this case, for the first mode  $\tau_R$  is about 10 years, whereas  $\tau_D$  is about 300 years, and they are comparable for the third mode, consistent with our result. Since the ratio  $\tau_D/\tau_R$  is proportional to the fourth power of the propagation speed of gravity waves, its sensitivity to the other parameters is small.

Although the zonal flows of the OGCM and those of the semianalytical solution are similar in basic pattern, there are still discrepancies; that is, the responses of the gravest modes for the semianalytical solution seem to be larger than those for the OGCM (cf. [Fig. 13a](#) with [Fig. 11](#)). This may be resolved by including horizontal diffusion. [Figure 14](#) shows the meridional section of the zonal flows when horizontal diffusion is introduced into [Eq. \(15\)](#). To obtain analytical solutions horizontal diffusion is estimated as

$$K_h \nabla^2 \eta \sim -K_h \frac{(2\pi)^2}{\lambda^2} \eta, \quad (27)$$



with use of the meridional scale of the wind forcing ( $\lambda$ ), where  $K_h$  is the coefficient of horizontal diffusion and  $\nabla$  is the horizontal gradient operator. We set  $K_h = 5.0 \times 10^2 \text{ m}^2 \text{ s}^{-1}$ . [Figure 14](#) captures the characteristics of [Fig. 11](#). When horizontal diffusion is introduced, the responses of the gravest modes, in particular the first and second modes, which are not affected much by vertical diffusion, become smaller. So especially at high latitudes, the barotropic mode dominates in the deep layer, as also seen in the OGCM experiments.

## 2) REDUCED-GRAVITY MODEL

There are still discrepancies in pattern between [Figs. 11 and 14](#) along the northern boundary and at lower latitudes ( $\sim 20^\circ\text{N}$ ). They seem to be due to Kelvin waves, which are induced by incident Rossby waves at the western boundary (e.g., [Milliff and McWilliams 1994](#)). The effects of the western boundary are not included in solution (21). Besides, the presentation of horizontal diffusion (27) may not be exact. To resolve the issues, we obtain numerical solutions to the shallow water wave equations using a  $1^\circ \times 1^\circ$  reduced-gravity model. The basic equations of the model for the  $n$ th mode are

$$\frac{\partial \tilde{u}_n}{\partial t} - f \tilde{v}_n = -g \frac{\partial \tilde{\eta}_n}{\partial x} + A_h \nabla^2 \tilde{u}_n + \tilde{F}_n, \quad (28)$$

$$\frac{\partial \tilde{v}_n}{\partial t} + f \tilde{u}_n = -g \frac{\partial \tilde{\eta}_n}{\partial y} + A_h \nabla^2 \tilde{v}_n + \tilde{G}_n, \quad (29)$$

$$\frac{\partial \tilde{\eta}_n}{\partial t} + H_n \left( \frac{\partial \tilde{u}_n}{\partial x} + \frac{\partial \tilde{v}_n}{\partial y} \right) = -\frac{K_v N^2}{c_n^2} \tilde{\eta}_n + K_h \nabla^2 \tilde{\eta}_n, \quad (30)$$

where  $A_h$  is the coefficient of horizontal viscosity. We set  $A_h = 2.3 \times 10^4 \text{ m}^2 \text{ s}^{-1}$ . The other parameters are the same as those used to solve [Eqs. \(13\), \(14\), and \(15\)](#). [Figure 15](#) depicts superposition (8) of the numerical solutions at a steady state for  $K_h = 0$  and  $K_h = 5.0 \times 10^2 \text{ m}^2 \text{ s}^{-1}$ . The superposition is made from the  $n = 0$  mode to the 20th mode. [Figure 15a](#) corresponds to [Fig. 13a](#). [Figure 15b](#) captures the characteristics of [Fig. 11](#), that is, the reversal of flow direction at the northern boundary and the response south of  $20^\circ\text{N}$  are also reproduced, although the amplitude in [Fig. 15b](#) is slightly weaker than that of the OGCM. This northern boundary flow is due to the boundary effect. It is confirmed that the inclusion of horizontal diffusion results in better similarity to the OGCM solution. The weaker zonal flows may be due to the difference in expression of vertical diffusion.

### d. Sensitivity to vertical and horizontal diffusion

We also carry out additional sensitivity experiments changing the vertical and horizontal diffusivities ([Table 1](#)). The OGCM is used because the profile of vertical diffusivity for the semianalytical analysis is constrained to be inversely proportional to  $N^2$  to enable the vertical mode decomposition.

For the vertical diffusivity, three experiments are carried out. In experiments S-V (small vertical diffusivity) and L-V (large vertical diffusivity), the vertical diffusivity is constant and is set to  $1.0 \times 10^{-5} \text{ m}^2 \text{ s}^{-1}$  and  $5.0 \times 10^{-4} \text{ m}^2 \text{ s}^{-1}$ , respectively. In experiment G-V (GFDL-type vertical diffusivity), the vertical diffusivity is taken as

$$\left\{ 7.0 + \frac{12.5}{\pi} \tan^{-1}[4.5 \times 10^{-3}(z - 2500)] \right\} \times 10^{-5} \quad (\text{m}^2 \text{ s}^{-1}). \quad (31)$$

This yields  $1.0 \times 10^{-5} \text{ m}^2 \text{ s}^{-1}$  in the upper layer and  $1.3 \times 10^{-4} \text{ m}^2 \text{ s}^{-1}$  in the deep layer, with a sharp change at 2500-m depth.

In the OGCM, GM-parameterization serves as wave damping. In experiment H-D (horizontal diffusivity instead of GM parameterization), the GM parameterization is not included but the horizontal diffusivity is set to  $7.0 \times 10^2 \text{ m}^2 \text{ s}^{-1}$ . In experiment S-G (small GM-parameterization), the coefficient of the GM parameterization is set to 0. The background

horizontal diffusivity is the same as in the control experiment. In experiment M-G (medium GM parameterization), the coefficient of GM parameterization is halved (set to  $3.5 \times 10^2 \text{ m}^2 \text{ s}^{-1}$ ). Apart from the parameters mentioned above, these experiments are carried out under the same conditions used in [section 3a](#).

[Figure 16](#) shows the meridional sections for the zonal flows along  $90^\circ\text{W}$ . When the small vertical diffusivity is used (experiment S-V), the higher modes cancel one another at depths below the thermocline, resulting in weak middepth zonal flows ([Fig. 16a](#)). On the other hand, when large vertical diffusivity is used (expt L-V), the flow is mainly composed of the first baroclinic mode at middle and high latitudes ([Fig. 16b](#)).

The GFDL-type vertical diffusivity [[Eq. \(31\)](#)] has a small value at depths above 2500 m. Although the higher modal structure becomes relatively weaker in the Tropics than the control case, [Fig. 16c](#) is similar to [Fig. 16b](#), indicating that the vertical diffusivity at the lower thermocline depths is important for Rossby wave damping.

[Figure 16d](#) confirms that GM parameterization and horizontal diffusion both damp Rossby waves. When GM parameterization is completely cut off ([Fig. 16d](#)), the pattern is quite similar to [Figs. 13a and 15a](#) as was expected. When the coefficient of GM parameterization is halved, the slant of the pattern becomes slightly gentler than control case ([Fig. 16e](#)), indicating that the sensitivity to the GM parameterization (horizontal diffusion) is low as long as it has a typical value.

The efficiencies of vertical and horizontal diffusion for damping the  $n$ th mode are  $\sim 1/C_n^4$  and  $\sim 1/C_n^2$ , respectively. Thus, roughly speaking, the use of large vertical diffusivity leads to the predominance of the first baroclinic mode response because the higher modes are quickly damped but the first mode is less altered. On the other hand, the use of horizontal diffusivity results in the predominance of the barotropic mode response because the gravest modes as well as the higher modes are damped.

#### 4. Discussion and concluding remarks

A series of middepth zonal flows has been reproduced in a  $1^\circ \times 1^\circ$  World Ocean model. The middepth zonal flows are shown to be created to the wind-driven circulation, which reaches down to several thousand meters. The surface wind gyres appear to shift poleward with depth, leaving behind the gyres that originate from the equatorial response. These gyres at middepths are similar to [Reid's \(1997\)](#) adjusted steric height maps. In the meridional sections, the distribution of the zonal flows shows that the pattern slants poleward with increasing depth. The formation mechanism for the middepth zonal flows is clarified using an idealized basin model and a semianalytical model of vertical normal mode decomposition. In the models the inclusion of vertical diffusion is essential. The zonal flows at low latitudes ( $10^\circ\text{S} \sim 10^\circ\text{N}$ ) are formed as the equatorial response to uniform zonal winds, which was already studied by [McCreary \(1981\)](#) and [Kitamura and Suginozono \(1987\)](#). The response at middle and high latitudes is accounted for as follows. Quasigeostrophic dynamics with vertical diffusion reproduces the reversal of the zonal flows with depth. For the higher modes, the Coriolis term owing to the meridional flow must be balanced by the local wind stress owing to the lack of zonal pressure gradient because Rossby waves from the eastern boundary do not propagate farther to the west. The slanting pattern is due to this non-QG diffusive solution, [\(23\)](#), for the higher modes. Then the inclusion of horizontal diffusion reduces the responses of the gravest modes, yielding better similarity to the OGCM solution. The third to fifth modes are very important for forming the middepth wind-driven circulation. The wind-driven circulation is certainly very weak compared to that in the surface layer, but this is sufficient to overcome the weak thermohaline circulation in the middepth Pacific. In summary, when weak flows below the thermocline are discussed, an assumption of a motionless abyssal layer is not appropriate even for the response to the wind forcing. This is because the introduction of vertical diffusion inevitably creates significant motion in the abyssal layers.

The vertical diffusivity used here seems large compared with the observed diffusivities at thermocline depth. But there is evidence that vertical diffusivity in the deep ocean is considerably enhanced over rough bathymetry (e.g., [Polzin et al. 1997](#)). When the locally enhanced large vertical diffusivity is taken into account, the net effect of the vertical diffusion may yield such a large value ([Morris et al. 1997](#)). In addition, the large diffusivity at the lower thermocline depths is needed to reproduce the assessed northward transport of Circumpolar Deep Water in the Pacific ([Tsujino et al. 2000](#)).

A series of middepth zonal flows appears when the magnitude of the wind-driven eastward flow exceeds that of the thermohaline westward flow around  $20^\circ$ . Otherwise, the eastward flows do not appear at these latitudes. The inclusion of the high-accuracy tracer advection scheme (UTOPIA) in the model and hence better representation of the pressure field may be of advantage to produce the middepth zonal flows. They should have signals in the existing models with moderate resolution of  $1^\circ \sim 2^\circ$ . In fact, a closer look at [Ishizaki's \(1994\)](#) horizontal pressure field yields their subtle signals. Since the middepth zonal flows are basically wind driven, they may also appear in the Atlantic, where the thermohaline circulation is very different. [Talley and Johnson \(1994\)](#) indicate westward flow between  $5^\circ\text{N}$  and  $8^\circ\text{N}$  and between  $10^\circ\text{S}$  and  $15^\circ\text{S}$ . Our result shows weak and broad westward flows between  $3^\circ$  and  $10^\circ$  in both hemispheres.

There are differences between Reid's (1997) steric height map and the modeled flow field, in particular, in the western Pacific, although the gross feature of the middepth zonal flows derived by Reid (1997) and Lupton (1998) is reproduced in the model. The difference is rather conspicuous for the lower thermocline depth ( $\sim 1000$  m). This is partly because the effects of mesoscale eddies such as homogenization of potential vorticity (e.g., Rhines and Young 1982) are not explicitly taken into account. When included, swift zonal flow may take place around the edge of the homogenized region (Nishino and Minobe 2000).

In addition, a closer look reveals differences in the eastern Pacific. In the eastern Tropics, Reid's (1997) steric height map shows zonally uniform flows, whereas the modeled flows have the Rossby dispersion pattern. Also at midlatitudes, Reid's (1997) steric height map shows broad eastward flow between  $20^\circ$  and  $40^\circ\text{N}$  from 1000 db to 3000 db whereas the modeled eastward flow is confined to between  $20^\circ$  and  $30^\circ\text{N}$ . The former discrepancy may be resolved by introducing the locally enhanced vertical diffusivity, which is small in the flat northeast Pacific, and large in the rough western Pacific and along the continental shelf (Samelson 1998; Hasumi and Sugimoto 1999b). The latter seems to be more difficult to solve. When the horizontal diffusion (GM parameterization) is reduced, as shown in Fig. 16f, the slant of the pattern becomes gentle and the eastward flow shifts northward. Nakano and Sugimoto (2001a) carried out an experiment where the GM parameterization is not introduced. The flow pattern is similar to experiment S-G. Although the eastward flow at midlatitudes shifts northward, the experiment with GM parameterization has a better resemblance to Reid's (1997) map on the whole.

In the observations, the middepth zonal flows are identified by the subtle tracer distribution. But ironically, the subtle distribution is not reproduced in the model while the zonal flows are clearly seen. The temperature and salinity fields only indicate the thermohaline circulation, whereas Talley and Johnson (1994) found the westward and eastward tongues in the temperature and salinity fields. This may be due to insufficient model resolution or excessively strong diffusion. For further understanding, including the effects of mesoscale eddies, an experiment using an eddy-resolving model is desired.

### Acknowledgments

We would like to thank Ryo Furue and Hiroyasu Hasumi for helpful comments and fruitful discussions. Thanks are extended to Tony Busalacchi, Eric Firing, Greg Johnson, Atsushi Kubokawa, Lynne Talley, and Mizuki Tsuchiya for pleasant discussions. Comments from two anonymous reviewers were helpful in improving the manuscript. The numerical experiments were performed on SR8000 at the Information Technology Center, University of Tokyo.

---

## REFERENCES

- Bryan K., 1984: Accelerating the convergence to equilibrium of ocean-climate model. *J. Phys. Oceanogr*, **14**, 666–673. [Find this article online](#)
- Danabasoglu G., J. C. McWilliams, and W. G. Large, 1996: Approach to equilibrium in accelerated global oceanic models. *J. Climate*, **9**, 1092–1110. [Find this article online](#)
- da Silva A. M., C. C. Young, and S. Levitus, 1994: *Atlas of Surface Marine Data 1994*. Vol. 1: *Algorithms and Procedures*, NOAA Atlas NESDIS 6, U.S. Govt. Printing Office, 83 pp..
- Davis R. E., 1998: Preliminary results from directly measuring middepth zonal circulation in the tropical and South Pacific. *J. Geophys. Res*, **103**, 24619–24639. [Find this article online](#)
- Firing E., 1987: Deep zonal currents in the central equatorial Pacific. *J. Mar. Res*, **45**, 791–812. [Find this article online](#)
- Furue R., 2001: An equatorial diffusive boundary layer and the equatorial stacked jets in thermally driven OGCMs. *J. Phys. Oceanogr*, **31**, 2737–2748. [Find this article online](#)
- Gent P. R., and J. C. McWilliams, 1990: Isopycnal mixing in ocean circulation models. *J. Phys. Oceanogr*, **20**, 150–155. [Find this article online](#)
- Haney R. L., 1971: Surface thermal boundary condition for ocean circulation models. *J. Phys. Oceanogr*, **1**, 241–248. [Find this article online](#)
- Hasumi H., 2000: Center for Climate System Research (CCSR) Ocean Component (COCO). CCSR Report No. 13, 68 pp.
- Hasumi H., and N. Sugimoto, 1999a: Sensitivity of a global ocean general circulation model to tracer advection schemes. *J. Phys. Oceanogr*, **29**, 2730–2740. [Find this article online](#)
- Hasumi H., and N. Sugimoto, 1999b: Effects of locally enhanced vertical diffusivity over rough bathymetry on the World Ocean

circulation. *J. Geophys. Res.*, **104**, 23367–23374. [Find this article online](#)

Hautala S. L., and S. C. Riser, 1993: A nonconservative  $\beta$ -spiral determination of the deep circulation in the eastern South Pacific. *J. Phys. Oceanogr.*, **23**, 1975–2000. [Find this article online](#)

Hellerman S., and M. Rosenstein, 1983: Normal monthly wind stress over the World Ocean with error estimates. *J. Phys. Oceanogr.*, **13**, 1093–1104. [Find this article online](#)

Ishizaki H., 1994: A simulation of the abyssal circulation in the North Pacific Ocean. Part I: Flow field and comparison with observations. *J. Phys. Oceanogr.*, **24**, 1921–1939. [Find this article online](#)

Johnson G. C., and J. M. Toole, 1993: Flow of deep and bottom water in the Pacific at 10°N. *Deep-Sea Res.*, **40**, 371–394. [Find this article online](#)

Killworth P. D., 1996: Time interpolation of forcing fields in ocean models. *J. Phys. Oceanogr.*, **26**, 136–143. [Find this article online](#)

Kitamura Y., and N. Suginohara, 1987: Effect of vertical viscosity and diffusivity on tropical ocean circulation. *J. Oceanogr. Soc. Japan*, **43**, 1–20. [Find this article online](#)

Leonard B. P., M. K. MacVean, and A. P. Lock, 1993: Positivity-preserving numerical schemes for multidimensional advection. NASA Tech. Memo. 106055, ICOMP-93-05, 62 pp.

Leonard B. P., M. K. MacVean, and A. P. Lock, 1994: The flux-integral method for multidimensional convection and diffusion. NASA Tech. Memo. 106679, ICOMP-94-13, 27 pp.

Levitus S., and T. P. Boyer, 1994: *World Ocean Atlas 1994*. Vol. 4: *Temperature*, NOAA Atlas NESDIS 4, 117 pp.

Lupton J., 1998: Hydrothermal helium plumes in the Pacific Ocean. *J. Geophys. Res.*, **103**, 15853–15868. [Find this article online](#)

McCreary J., 1981: A linear stratified ocean model of the equatorial undercurrent. *Philos. Trans. Roy. Soc. London*, **298**, 603–635.

Milliff R. F., and J. C. McWilliams, 1994: The evolution of boundary pressure in ocean basins. *J. Phys. Oceanogr.*, **24**, 1317–1338. [Find this article online](#)

Morris M., N. G. Hogg, and W. B. Owens, 1997: Diapycnal mixing estimated from advective budgets in the deep Brazil Basin. *WOCE Newsl.*, **28**, 23–25. [Find this article online](#)

Nakano H., and N. Suginohara, 2001: Importance of the eastern Indian for the abyssal Pacific. *J. Geophys. Res.*, submitted.

Nakano H., and N. Suginohara, 2002: Effects of bottom boundary layer parameterization on reproducing deep and bottom waters in a World Ocean model. *J. Phys. Oceanogr.*, in press.

Nishino S., and S. Minobe, 2000: Buoyancy- and wind-driven circulation in an extended model of potential vorticity homogenization. *J. Phys. Oceanogr.*, **30**, 2391–2403. [Find this article online](#)

Obata A., R. Furue, S. Aoki, and N. Suginohara, 1996: Modeling layered structure in deep Pacific circulation. *J. Geophys. Res.*, **101**, 3663–3674. [Find this article online](#)

Polzin K. L., J. M. Toole, J. R. Ledwell, and R. W. Schmitt, 1997: Spatial variability of turbulent mixing in the abyssal ocean. *Science*, **276**, 93–96. [Find this article online](#)

Reid J. L., 1997: On the total geostrophic circulation of the Pacific Ocean: Flow patterns, tracers, and transports. *Progress in Oceanography*, Vol. 39, Pergamon, 263–352.

Rhines P. B., and W. R. Young, 1982: A theory of the wind-driven circulation. I. Mid-ocean gyres. *J. Mar. Res.*, **40**, 559–596, (Suppl). [Find this article online](#)

Roemmich D., S. Hautala, and D. Rudnick, 1996: Northward abyssal transport through the Samoan passage and adjacent regions. *J. Geophys. Res.*, **101**, 14039–14055. [Find this article online](#)

Samelson R. M., 1998: Large-scale circulation with locally enhanced vertical mixing. *J. Phys. Oceanogr.*, **28**, 712–726. [Find this article online](#)

Speer K., E. Tziperman, and Y. Feliks, 1993: Topography and grounding in a simple bottom layer model. *J. Geophys. Res.*, **98**, 8547–8558. [Find this article online](#)

Stommel H., 1982: Is the South Pacific helium-3 plume dynamically active? *Earth Planet. Sci. Lett.*, **61**, 63–67. [Find this article online](#)

Stommel H., and A. B. Arons, 1960a: On the abyssal circulation of the world ocean—I. Stationary planetary flow patterns on a sphere. *Deep-Sea Res*, **6**, 140–154. [Find this article online](#)

Stommel H., and A. B. Arons, 1960b: On the abyssal circulation of the World Ocean—II. An idealized model of the circulation pattern and amplitude in oceanic basins. *Deep-Sea Res*, **6**, 217–223. [Find this article online](#)

Suginohara N., and M. Fukasawa, 1988: Set-up of deep circulation in multi-level numerical models. *J. Oceanogr. Soc. Japan*, **44**, 315–336. [Find this article online](#)

Suginohara N., and S. Aoki, 1991: Buoyancy-driven circulation as horizontal convection on  $\beta$  plane. *J. Mar. Res*, **49**, 295–320. [Find this article online](#)

Suginohara N., S. Aoki, and M. Fukasawa, 1991: Comments on “On the importance of vertical resolution in certain ocean general circulation models.”. *J. Phys. Oceanogr*, **21**, 1699–1701. [Find this article online](#)

Talley L. D., and G. C. Johnson, 1994: Deep, zonal subequatorial currents. *Science*, **263**, 1125–1128. [Find this article online](#)

Tsujino H., H. Hasumi, and N. Suginohara, 2000: Deep Pacific circulation controlled by vertical diffusivity at the lower thermocline depth. *J. Phys. Oceanogr*, **30**, 2853–2865. [Find this article online](#)

Warren B. A., and W. B. Owens, 1985: Some preliminary results concerning deep northern-boundary currents in the North Pacific. *Progress in Oceanography*, Vol. 14, Pergamon, 537–551.

Yamanaka Y., R. Furue, H. Hasumi, and N. Suginohara, 2000: Comparison of two classical advection schemes in a general circulation model. *J. Phys. Oceanogr*, **30**, 2439–2451. [Find this article online](#)

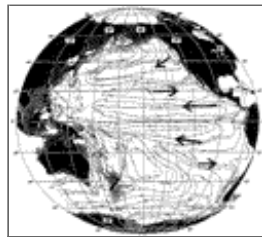
## Tables

TABLE 1. List of sensitivity experiments to vertical and horizontal diffusion

Expt	Vert diffusivity ( $\text{m}^2 \text{s}^{-1}$ )	Hor diffusivity ( $\text{m}^2 \text{s}^{-1}$ )	GM ( $\text{m}^2 \text{s}^{-1}$ )
Control (sec. 3 <sup>c</sup> )	Tsujino et al. (2000)	$1.0 \times 10^2$	$7.0 \times 10^2$
S-V	$1.0 \times 10^{-5}$	$1.0 \times 10^2$	$7.0 \times 10^2$
L-V	$5.0 \times 10^{-4}$	$1.0 \times 10^2$	$7.0 \times 10^2$
G-V	GFDL type [Eq. (31)]	$1.0 \times 10^2$	$7.0 \times 10^2$
H-D	Tsujino et al. (2000)	$7.0 \times 10^2$	0
S-G	Tsujino et al. (2000)	$1.0 \times 10^2$	0
M-G	Tsujino et al. (2000)	$1.0 \times 10^2$	$3.5 \times 10^2$

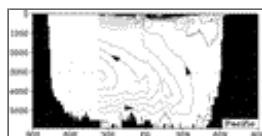
[Click on thumbnail for full-sized image.](#)

## Figures



[Click on thumbnail for full-sized image.](#)

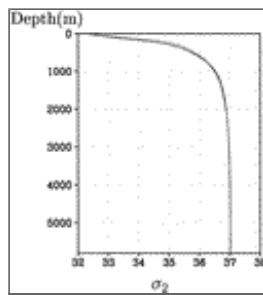
FIG. 1. Adjusted steric height at 2500 dbar from Reid (1997) in units of dynamic meters ( $10 \text{ m}^2 \text{ s}^{-2}$ ). Thick arrows indicate the location and sense of flow defined by the deep  $^3\text{He}$  fields (after Lupton 1998)



[Click on thumbnail for full-sized image.](#)

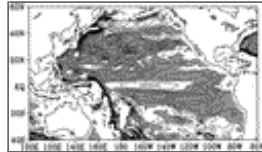
FIG. 2. Zonally integrated meridional transport streamfunction in the Pacific. The streamfunction includes the eddy-induced

transport. Contour interval is 2 Sv



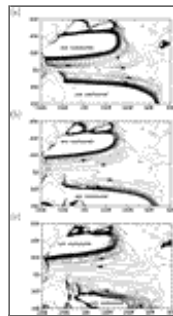
[Click on thumbnail for full-sized image.](#)

FIG. 3. Vertical profile of horizontally averaged potential density ( $\sigma_2$ ) in the North Pacific for the World Ocean model (solid line) and for the annual mean climatology of [Levitus and Boyer \(1994\)](#) (dotted line)



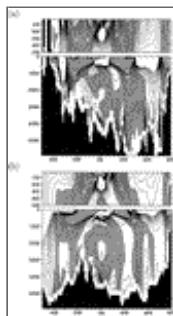
[Click on thumbnail for full-sized image.](#)

FIG. 4. Zonal flow at 2405-m depth in the Pacific. Contour interval is  $0.05 \text{ cm s}^{-1}$ . Shaded areas indicate westward flow



[Click on thumbnail for full-sized image.](#)

FIG. 5. Pressure fields in the Pacific at (a) 500, (b) 1000, and (c) 1500 m. Contour intervals are (a) 0.002 db, (b) 0.001 db, and (c) 0.0005 db



[Click on thumbnail for full-sized image.](#)

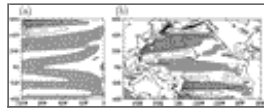
FIG. 6. Zonal flow along (a)  $170^\circ\text{E}$  and (b)  $140^\circ\text{W}$ . For the upper panels of (a) and (b), contour intervals are  $1 \text{ cm s}^{-1}$ , and for the lower panels,  $0.1 \text{ cm s}^{-1}$ . In the upper panels, contours are drawn between  $-10$  and  $10 \text{ cm s}^{-1}$ , and in the lower panels,  $-1$  and  $1 \text{ cm s}^{-1}$ . Shaded areas indicate westward flow



[Click on thumbnail for full-sized image.](#)

FIG. 7. Difference in zonal flow between the cases with and without Pacific winds for the World Ocean model (wind-no-wind) along (a)  $170^\circ\text{E}$  and (b)  $140^\circ\text{W}$ . Contour interval is  $0.1 \text{ cm s}^{-1}$ . Contours are drawn between  $-1$  and  $1 \text{ cm s}^{-1}$ . Shaded areas

indicate westward flow



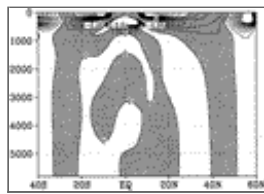
[Click on thumbnail for full-sized image.](#)

FIG. 8. (a) Zonal flow at 2405-m depth in the rectangular basin model. (b) Difference in zonal flow between the cases with and without Pacific winds for the World Ocean model (wind–no-wind). Contour interval is  $0.05 \text{ cm s}^{-1}$ . Shaded areas indicate westward flow



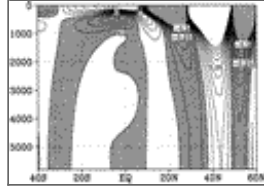
[Click on thumbnail for full-sized image.](#)

FIG. 9. Zonal flow for the rectangular basin model along (a)  $90^\circ\text{W}$  and (b)  $30^\circ\text{W}$ . Contour interval is  $0.05 \text{ cm s}^{-1}$ . Contours are drawn between  $-0.5$  and  $0.5 \text{ cm s}^{-1}$ . Shaded areas indicate westward flow



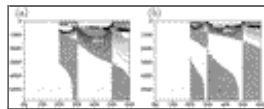
[Click on thumbnail for full-sized image.](#)

FIG. 10. Zonal flow along  $90^\circ\text{W}$  when uniform zonal winds are imposed. Contour interval is  $0.05 \text{ cm s}^{-1}$ . Contours are drawn between  $-0.5$  and  $0.5 \text{ cm s}^{-1}$ . Shaded areas indicate westward flow



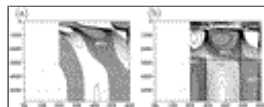
[Click on thumbnail for full-sized image.](#)

FIG. 11. Same as [Fig. 10](#) but when the zonal wind stress,  $(1)$ , is imposed



[Click on thumbnail for full-sized image.](#)

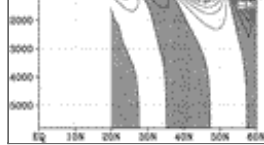
FIG. 12. Zonal flow for QG equations along (a)  $90^\circ\text{W}$  and (b)  $30^\circ\text{W}$ . Contour interval is  $0.05 \text{ cm s}^{-1}$ . Contours are drawn between  $-0.5$  and  $0.5 \text{ cm s}^{-1}$ . Shaded areas indicate westward flow. Note that the latitudinal scale is enlarged compared with that of [Fig. 11](#) to show details of the slanting pattern



[Click on thumbnail for full-sized image.](#)

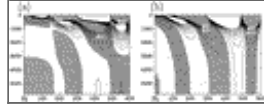
FIG. 13. (a) Zonal flow for the shallow water wave equations along  $90^\circ\text{W}$ . Contour interval is  $0.05 \text{ cm s}^{-1}$ . Contours are drawn between  $-0.5$  and  $0.5 \text{ cm s}^{-1}$ . Shaded areas indicate westward flow. (b) Same as (a) but the sum of the barotropic mode and the first and second baroclinic modes (the shaded areas indicate westward flow). The thick contour represents the third baroclinic mode (the dotted contours indicate westward flow). Note that the latitudinal scale is enlarged compared with that of [Fig. 11](#)





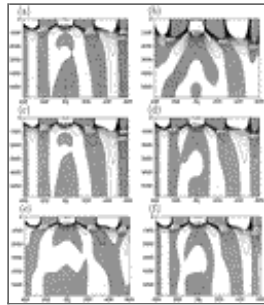
Click on thumbnail for full-sized image.

FIG. 14. Same as [Fig. 13a](#) but including horizontal diffusion



Click on thumbnail for full-sized image.

FIG. 15. Zonal flow for the superposition of the numerical solutions along  $90^\circ\text{W}$ . The superposition is made from the  $n = 0$  mode to the 20th mode. (a)  $K_h = 0$  and (b)  $K_h = 5 \times 10^2 \text{ m}^2 \text{ s}^{-1}$ . Contour interval is  $0.05 \text{ cm s}^{-1}$ . Contours are drawn between  $-0.5$  and  $0.5 \text{ cm s}^{-1}$ . Shaded areas indicate westward flow. Note that the latitudinal scale is enlarged compared with that of [Fig. 11](#)



Click on thumbnail for full-sized image.

FIG. 16. Zonal flow for the rectangular basin model along  $90^\circ\text{W}$  for (a) S-V, (b) L-V, (c) G-V, (d) H-D, (e) S-G, and (f) M-G (for the parameters, see [Table 1](#)). Contour interval is  $0.05 \text{ cm s}^{-1}$ . Contours are drawn between  $-0.5$  and  $0.5 \text{ cm s}^{-1}$ . Shaded areas indicate westward flow

\* Current affiliation: Center for Ocean-Atmospheric Prediction Studies, The Florida State University, Tallahassee, Florida.

Corresponding author address: Dr. Nakano Hideyuki, Center for Climate System Research, University of Tokyo, 4-6-1 Komaba, Meguro-ku, Tokyo 153-8904, Japan. E-mail: [nakano@ccsr.u-tokyo.ac.jp](mailto:nakano@ccsr.u-tokyo.ac.jp)

top ▲



© 2008 American Meteorological Society [Privacy Policy and Disclaimer](#)  
 Headquarters: 45 Beacon Street Boston, MA 02108-3693  
 DC Office: 1120 G Street, NW, Suite 800 Washington DC, 20005-3826  
[amsinfo@ametsoc.org](mailto:amsinfo@ametsoc.org) Phone: 617-227-2425 Fax: 617-742-8718  
[Allen Press, Inc.](#) assists in the online publication of AMS journals.